CrossMark

RESEARCH ARTICLE

Signal-to-noise ratio improvements in laser flow diagnostics using time-resolved image averaging and high dynamic range imaging

Davide Giassi[1] ◉ · **Marshall B. Long[1]**

Abstract Two alternative image readout approaches are demonstrated to improve the signal-to-noise ratio (SNR) in temporally resolved laser-based imaging experiments of turbulent phenomena. The first method exploits the temporal decay characteristics of the phosphor screens of image intensifiers when coupled to an interline-transfer CCD camera operated in double-frame mode. Specifically, the light emitted by the phosphor screen, which has a finite decay constant, is equally distributed and recorded over the two sequential frames of the detector so that an averaged image can be reconstructed. The characterization of both detector and image intensifier showed that the technique preserves the correct quantitative information, and its applicability to reactive flows was verified using planar Rayleigh scattering and tested with the acquisition of images of both steady and turbulent partially premixed methane/air flames. The comparison between conventional Rayleigh results and the averaged ones showed that the SNR of the averaged image is higher than the conventional one; with the setup used in this work, the gain in SNR was seen to approach 30 %, for both the steady and turbulent cases. The second technique uses the two-frame readout of an interline-transfer CCD to increase the image SNR based on high dynamic range imaging, and it was tested in an unsteady non-reactive flow of Freon-12 injected in air. The result showed a 15 % increase in the SNR of the low-pixel-count regions of an image, when compared to the pixels of a conventionally averaged one.

✉ Davide Giassi
davide.giassi@yale.edu

[1] Department of Mechanical Engineering and Materials Science, Yale University, 15 Prospect St., New Haven, CT 06511, USA

1 Introduction

Laser-based imaging diagnostics such as Rayleigh scattering or laser-induced fluorescence are used extensively for studying reacting and non-reacting flows and can provide quantitative, non-intrusive measurements of chemical species concentration, gas density and/or temperature (Eckbreth 1996; Kaminski and Long 2002; Miles and Lempert 1990). Practical limitations affecting the quality of the collected data might include the finite dynamic range of the detectors and the limited signal-to-noise ratios (SNR) of the measurements; inherent noise sources, such as shot, dark and readout noise can, in fact, adversely affect the measurements (Janesick 2001). Numerous post-processing denoising techniques have been developed to reduce image noise, albeit with the risk of loosing spatial accuracy; recent reviews of existing denoising methods are presented in Shao et al. 2014; Jain et al. 2014; Irum et al. 2015. In some cases, the SNR can be improved by averaging multiple acquisitions or, as recently demonstrated in steady combustion systems, by implementing high dynamic range imaging (Giassi et al. 2015). This, however, can be problematic in those situations when conventional averaging or phase-locked measurements cannot be implemented, such as with imaging of turbulent flows. The scope of the first part of this work is to demonstrate a technique that would allow an increase in the SNR in images of unsteady flows, where the aforementioned conventional averaging, or the implementation of HDR imaging, is in general not possible. Without any additional increase in hardware complexity, the approach could prove valuable in those experimental setups designed for the time-resolved characterization of turbulent flows, in which image intensifiers are used either to increase the intensity of weak signals or as fast gating devices.

In general, image intensifiers operate by converting low levels of light into electrons (through a photocathode, via the photoelectric effect), accelerating those electrons with microchannel plates (MCP), amplifying them through secondary cascade emission when the electrons hit the MCP, and finally converting them back into photons when they strike a phosphor screen at the back end of the intensifier. The idea behind this work exploits the inherent behavior of these devices and relies on the finite temporal decay of the phosphor emission. By using the capability of interline-transfer CCD cameras to acquire two sequential images with a short interframe temporal separation, it is possible to collect the phosphor-emitted light over the two consecutive frames and use them to perform an averaging that comprises two images. Despite the phosphor temporal decay being relatively slow, thus limiting the measurement repetition rate (in this work, the intensifier phosphor light reached 5 % of its peak value after ~50 μs), the minimum time scales that are resolvable are still determined by the length of the laser pulse (order of ns).

To prove the validity of the concept and its possible application to real experimental conditions, this work uses planar Rayleigh imaging to acquire and compare the SNR from two different sets of images of a partially premixed methane/air flame. Data were obtained first using the conventional Rayleigh imaging approach, where the total Rayleigh-scattered light is collected in a single image; this result served as a reference and provided a baseline to which the SNR of the new approach could be compared. A second dataset was obtained using the two-image averaging technique. To avoid uncertainties in the interpretation of results associated with the variable nature of the turbulent features, datasets were first collected in a steady flame and then extended to a turbulent one.

Finally, an alternative method to enhance the image SNR, based on high dynamic range imaging (Giassi et al. 2015), is demonstrated on a simplified unsteady flow of Freon-12 injected in air, and the SNR of the reconstructed HDR image compared to that of a conventionally averaged image.

2 Experimental setup

In Rayleigh imaging, the signal S_{Ray} that is collected by a detector can be expressed as in Eq. (1),

$$S_{Ray} = KE_0 NV \sum_i x_i \sigma_i \tag{1}$$

where K is the efficiency of the collection optics, E_0 the laser single shot energy, N the number density, and V the collection volume. In the summation term (called the effective Rayleigh cross section), x_i and σ_i are the mole fraction

and Rayleigh cross section of the ith chemical species, respectively (Zhao and Hiroyasu 1993). Rayleigh scattering can be used to determine species concentration in the case of isothermal mixing or, given information on the effective Rayleigh cross section, for temperature measurements through the inverse relationship with N (Zhao and Hiroyasu 1993). In Rayleigh thermometry, the signal reaches its minimum at the flame front, where the temperature is the highest; the resulting low SNR of this region may be a limitation in the accuracy of the measurement. For this reason, Rayleigh scattering is an ideal test case to show how low SNR values could be mitigated with the proposed two-image averaging.

The experimental configuration used to test the applicability of the approach to reactive flows is shown in Fig. 1 where an illuminating laser sheet is generated using a sheet-forming telescope and sent into the probe volume where the Rayleigh-scattered light is collected and imaged onto an interline-transfer CCD through a Gen III image intensifier.

The second harmonic of a Spectra Physics Pro-250 Nd:YAG laser was focused into a sheet (3.3-mm height, ~35-μm FWHM beam waist thickness—as determined by imaging the attenuated laser sheet onto a detector, 350 mJ/pulse, 10 Hz-repetition rate, 10-ns pulse length) and sent through a partially premixed methane flame (75 % air, 25 % CH_4 by volume, 4- and 2-mm nozzle diameter for the steady and turbulent flames, respectively) surrounded by an air co-flow (75-mm O.D. diameter, 35 cm/s average velocity). The beam focusing and sheet forming were achieved with a telescope comprising a 300-mm focal length spherical lens and a negative 100-mm focal length concave cylindrical lens. The beam height was decreased from 10 to 3.3 mm to match the detector chip size and increase the fluence. The average velocities of the fuel mixture were 2.6 m/s for the steady flame and 32 m/s for the turbulent flame, resulting in a jet Reynolds number of ~4000. A premixed methane pilot flame, in an arrangement co-annular
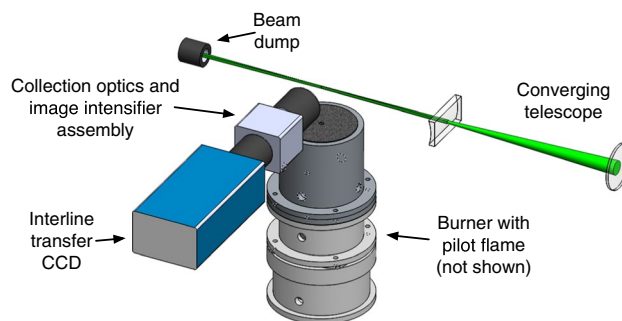

Fig. 1 Schematic drawing of the experimental setup, showing the detector, the collection optics, the burner, and the laser sheet forming optics

to the main jet (9.6 mm I.D., 13.3 mm O.D.), was added
to the burner to anchor the turbulent flame and avoid blow
off. The Rayleigh-scattered light was collected through
a pair of Nikkor 50-mm lenses and imaged onto the front
faceplate of an ITT Gen III MCP image intensifier (GaAs
photocathode, 18-mm diameter, 45 l p/mm, 1-μs gate time,
P20 phosphor, 5–10 V nominal gain voltage range) using
one-to-one magnification. The resulting intensified image
was then imaged onto the chip of a cooled SensiCam inter-
line-transfer CCD (1280×512 pixels—when operated in
double-frame mode, binned 2×2 pixels, 12 bit A/D con-
verter) using an additional pair of Nikkor 50-mm lenses
with one-to-one magnification. The measurements were
taken at a height above the burner (HAB) centered either at
six or twelve diameters downstream for the steady and tur-
bulent flames, respectively. Two Stanford Research DG535
pulse generators synchronized the laser, image intensifier
and camera. The intensifier gain voltages were matched to
the laser pulse energy and set to 6.5 and 7 V for the con-
ventional and averaged measurements, respectively, so that
the collected images used the same portion of the camera
dynamic range without any saturation. The light emitted
by the intensifier phosphors was recorded by the interline-
transfer CCD camera using the double-frame option; when
operated in this mode, the camera was able to record two
consecutive frames with a time separation of 1 μs. The
exposure could only be set for the first of the two frames,
with the exposure of the second image determined by the
speed of the CCD readout (measured to be 46.45 ms). For
the conventional Rayleigh measurement, the first exposure
was set to 50 ms in order for the first frame to collect all the
light emitted by the intensifier phosphors. Conversely, for
the averaged Rayleigh measurement, the exposure of the
first frame was reduced to 30 μs so that the integrated col-
lected light, thus the recorded counts, was equally divided
between the two frames.

Figure 2 shows the normalized intensity of the phosphor
light as function of time, as measured with a photomulti-
plier, and summarizes the relative delays between laser
pulse, intensifier gate, and camera exposures for the case of
the averaged acquisition. With reference to Fig. 2, the 10-ns
laser pulse (not shown) is centered at 0 μs, the 1-μs gate
time of the image intensifier is shown by the green square
wave, while the exposure of the first and second frames of
the interline-transfer CCD is shown by the red and orange
square waves, respectively. Note that the "tail" of the P20
phosphor decay continues up to ~50 ms (Hoess and Kar-
lheinz 2000; Proxitronic datasheet 1998) and the second
frame exposure continues up to 46.45 ms, but they are
truncated at 50 μs for ease of visualization. In general, P20
phosphors are characterized by a non-exponential decay
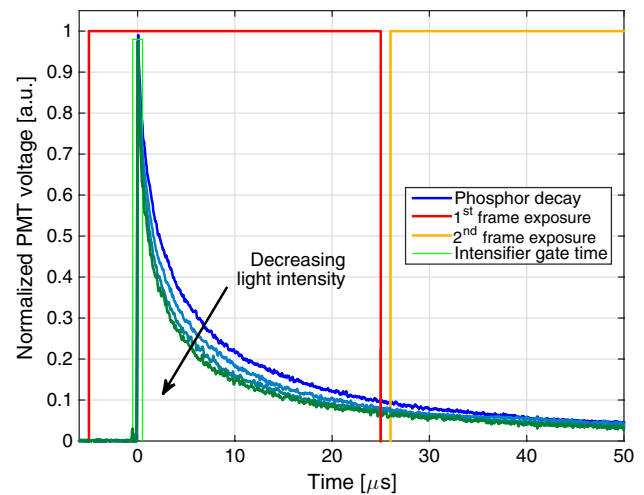with two distinct responses: an initial short-time behavior

Fig. 2 Normalized phosphor temporal decay, shown for decreasing light intensity, when compared to the image intensifier gate and Sen-siCam exposures

with a fast decay (which is the one shown in Fig. 2) fol-
lowed by a long-time behavior, which has a much slower
decay (Hoess and Karlheinz 2000). In this case, the char-
acteristic time constant of the intensifier decay, as well as
the CCD readout time, limits the measurements to repeti-
tion rates less than 20 Hz. The use of faster phosphors such
as P46 or P47 (Hoess and Karlheinz 2001), along with a
detector capable of faster readout, would allow for higher
repetition rates.

All steps of the acquisition process were controlled
using the open source software OMA (Kalt and Long 2014)
and, regardless of the approach followed (conventional or
averaged Rayleigh), each image was processed indepen-
dently using MATLAB. First, an offset subtraction (flame
images taken with the laser off) was performed to account
for fixed pattern camera noise and DC offset; the result was
then normalized with a Rayleigh-scattered image of air in
order to account for laser sheet non-uniformities; both off-
set and air images were the result of an average over ten
shots. The Rayleigh intensity of areas with uniform tem-
perature and gas composition is expected to be constant,
so a final horizontal "stripe correction" was implemented
to remove any remaining laser sheet non-uniformities. Each
image was rotated by 1° in order to align the stripes hori-
zontally and to account for the fact that the detector chip
was not parallel to the laser sheet direction. This operation
introduced additional pixels to the image, which was there-
fore clipped to 2.8 mm × 9.8 mm. For this correction, each
column of the image was normalized with an array whose
intensity was obtained by averaging, row by row, multiple
columns in an area of the image where only air was pre-
sent. Note that the rotation algorithm returned a slightly

smoothed image as a result of the implemented bicubic interpolation, which in turn somewhat decreased the original noise of the image.

3 Detector and image intensifier characterization

As in every quantitative imaging experiment, the meaningfulness of the data relies on the assumption that the detector is linear over its entire dynamic range. The linearity of the SensiCam used in this study has been verified following the methodology presented in (Giassi et al. 2015), where a pulsed LED was used as an illumination source and whose radiant energy was controlled by varying its gating time. The excellent linearity of the detector is shown by the green markers in Fig. 3a (the black line represents a perfect linear trend), where the solid and empty markers identify the response evaluated considering the first and second frames of the camera, respectively (when used in double-frame mode). The LED approach was not employed to verify the linearity of the image intensifier due to the relatively long LED exposures that could saturate and damage the intensifier itself. Instead, Rayleigh-scattered light of air was used as an illumination source and the phosphor-emitted light recorded using a Hamamatsu R928 photomultiplier connected to an Atten 100-MHz oscilloscope. The collected scattered light intensity was progressively decreased by means of neutral density filters, while both the photomultiplier and the image intensifier were operated at a fixed gain voltage (the intensifier gain was set to 7 V). Figure 3b shows the integrated signal recorded by the PMT as function of the neutral density filter transmittance
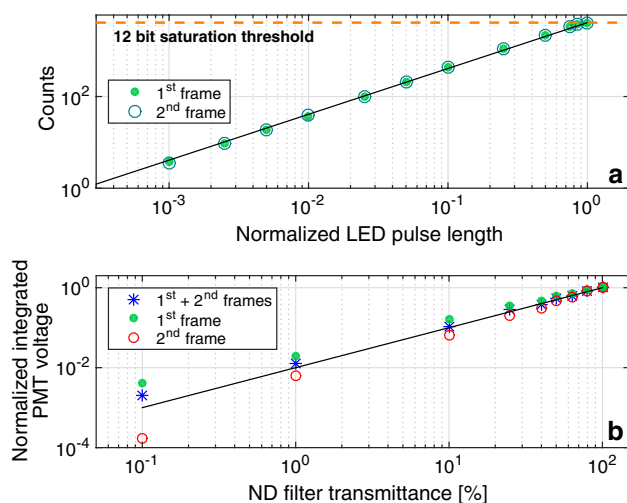

Fig. 3 a SensiCam linearity as determined by LED measurements. *Solid* and *empty markers* identify the first and second frames of the interline-transfer CCD, respectively. **b** Image intensifier linearity as determined by photomultiplier measurements

(blue markers). The linearity of the intensifier is seen to be excellent, and the largest signal measured with the photomultiplier (case with no ND filter), which corresponds to the largest signal in the Rayleigh temperature measurement, was taken as a reference, and the decay curve, similar to that shown in Fig. 2, was divided into two regions (with equal integrated voltages) to simulate the two sequential CCD exposures. The temporal splitting determined with the reference signal was maintained for all the remaining measurements and the resulting integrated voltages, for both "frames," are shown in Fig. 3b (green and red markers).

The small deviation of the individual frames that can be observed in Fig. 3b (as the neutral density filter transmittance is decreased) can be attributed to the fact that the normalized shape of the phosphor decay changes depending on the intensity of the incoming light, as shown in Fig. 2. If the temporal splitting between the two regions is kept constant, the ratio between the two integrated voltages deviates from unity as the normalized decay shapes start deviating from the reference one. As a consequence, it was seen that, if the camera exposures are set to equalize the high intensity counts, the low intensity ones can differ up to ~4 % of the detector full dynamic range. This discrepancy, however, will not affect the validity of the quantitative result; when evaluating the average, the counts of the two frames are added, and this, in turn, is equivalent to employing the conventional Rayleigh approach where all the light is recorded into a single frame (the subsequent division by 2 to obtain the average value is simply a normalization). The previous conclusion is true if the amount of light that is not recorded during the 1 μs interframe separation is negligible. The photomultiplier results let us indeed verify that the light that would be collected over the 1 μs window would account for less than 1 % of the total integrated light.

The SNR of the image returned by the phosphor screen also depends on the gain level of the device itself (Zhou et al. 2013); typically, the SNR response of an intensifier is linear up to a certain gain value, above which the SNR level reaches a plateau. To evaluate the intensifier SNR characteristics, Rayleigh-scattered images of dichlorodifluoromethane (which has a Rayleigh cross section ~20 times greater than that of air) were recorded as a function of the intensifier gain; the laser energy and the SensiCam exposure were kept constant, while the intensifier gain was varied in the range 6–9 V. To decouple the influence of the SNR characteristics of the detector on the final result, the recorded counts, regardless of the chosen intensifier gain, were kept constant (~2000 counts) by means of neutral density filters. In Fig. 4a, the solid markers represent the averaged counts of ten images, divided by the neutral density filter transmittance, evaluated in an interrogation
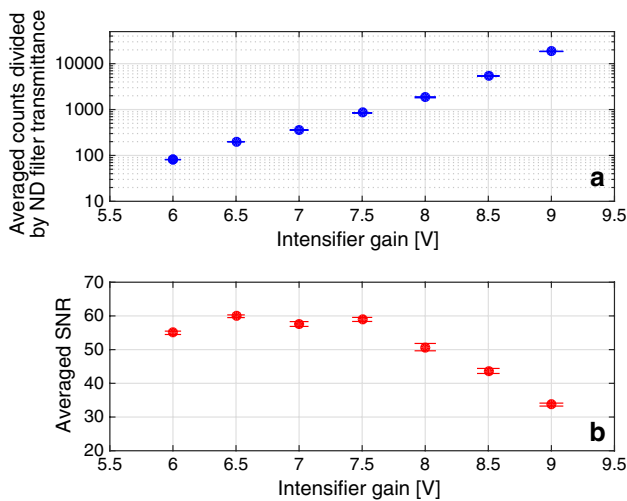
Fig. 4 **a** Average counts evaluated from Rayleigh scattering images of dichlorodifluoromethane, divided by the neutral density filter transmittance, and **b** SNR of those images as function of the image intensifier gain. The *error bars* identify the standard deviation over ten measurements

region where the recorded intensity was roughly constant, while the error bars identify the standard deviation.

The SNR of the image was evaluated according to the following procedure: An initial two-dimensional Gaussian smoothing was done to the image over an area with a $1/e^2$ full width of 14 pixels; then, in a two-dimensional 9 by 9 pixels sub-interrogation region centered around each pixel (see Fig. 5a), the SNR was calculated by dividing the average value of the sub-interrogation region by the root-mean-square of the difference between the region intensity and the "average" surface obtained with the initial smoothing.

Figure 4b shows the average SNR of the ten acquired images (solid marker) with the standard deviation identified by the error bars. Despite the recorded counts being kept constant, the SNR of the image remains unchanged only up to 7.5 V, above which the noise starts increasing causing a drop in the overall SNR. For this reason, the in-flame Rayleigh measurements were taken below the aforementioned threshold using a gain of 6.5 and 7 V for the conventional and averaged approaches, respectively. As shown in Fig. 4a, increasing the gain from 6.5 to 7 V doubles the light that is emitted by the intensifier (thus the counts recorded by the detector), which is necessary if the same detector dynamic range is used with the two approaches.

4 Results

As mentioned, the Rayleigh measurements were at first taken in a steady partially premixed methane/air flame to avoid the random variability of turbulent structures to affect the SNR evaluation. Figure 5a, b shows the Rayleigh signal (corrected for laser sheet non-uniformities) recorded in the flame using the conventional and averaged approach, respectively. The high-signal-count region on the right identifies the air side at ambient temperature, and the blue square displayed in Fig. 5a shows the size of the interrogation region used for the SNR evaluation, as introduced in Sect. 3.

Figure 5c, d shows the SNR distribution of the Rayleigh images collected using the conventional and average approaches, respectively, evaluated according to the procedure described in Sect. 3. As expected, the SNR of the averaged image is higher that the one obtained with the
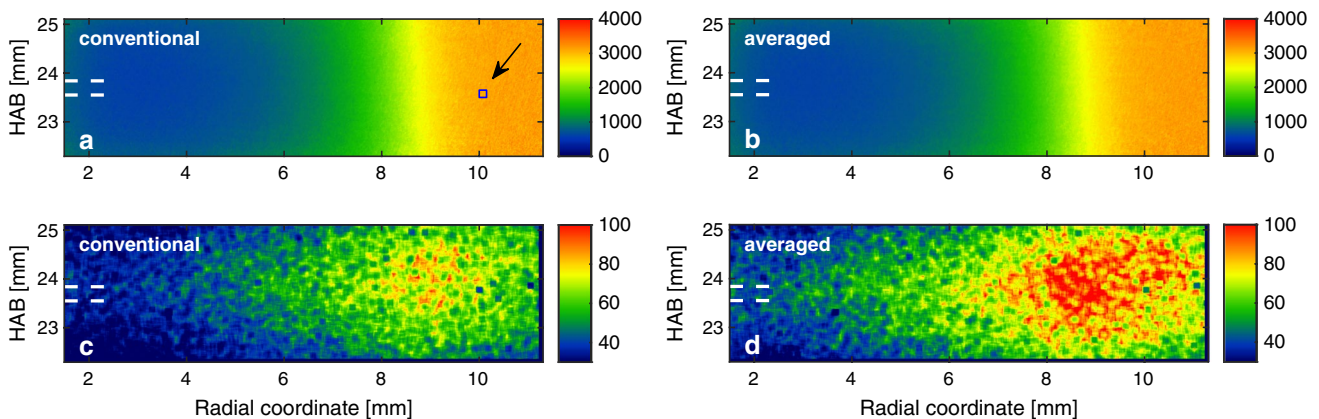

Fig. 5 **a** Rayleigh signal, in arbitrary units and corrected for laser sheet non-uniformities, of the conventional and **b** averaged Rayleigh images for the steady methane/air partially premixed flame. The *dashed lines* define a region over which the axial averaging has been performed to plot the *curves* shown in Fig. 6, while the *blue square*

pointed by the *arrow* shows the size of the interrogation region used for the SNR evaluation, as explained in Sect. 3. **c** SNR distribution of the conventional and **d** averaged Rayleigh images for the steady methane/air partially premixed flame
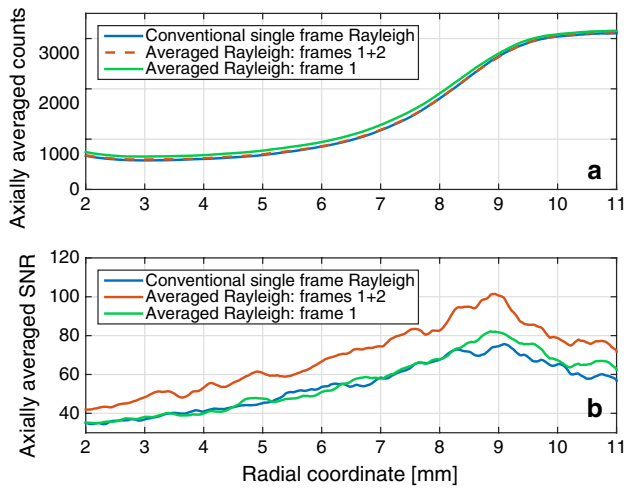
Fig. 6 **a** Comparison between the axially averaged Rayleigh counts and **b** the axially averaged SNR, for the steady partially premixed methane/air flame

conventional method, and the increase affects the whole image, regardless of the pixel value. Note that, in general, the SNR of an image tends to follow the signal intensity distribution before any correction is performed (shaped by the Gaussian energy distribution of the laser sheet along the image axial direction, as well as by image vignetting). Because of that, even though the corrected intensity of the Rayleigh-scattered light is relatively constant in some regions, the SNR is not and, as shown in Fig. 5c, d, its value decreases toward the upper and lower, as well as toward the left and right edges of the image. Figure 6 shows a comparison similar to the one presented in Fig. 5 by plotting the axially averaged counts of the corrected Rayleigh images (Fig. 6a) and the axially integrated SNR values (Fig. 6b) over a region defined by the white dashed lines shown in

Fig. 5. Given a comparable value of the recorded counts, for this particular example, the increase in SNR approached 30 %. The green curve shows the axially averaged SNR value when considering just the first of the two frames of the image sequence with a result that is, predictably, equivalent to the conventional Rayleigh one.

The proposed approach is able to increase the overall SNR by exploiting the fact that noise is a random process having a zero mean; the averaging of multiple different images tends to even out the random noise fluctuations. The theoretical SNR improvement, if shot noise is the main noise contribution, would be proportional to $\sqrt{2}$ (where two, in this case, is the number of images being averaged); however, in this work, the large number of scattered photons collected by the detector meant that the combination of dark, intensifier, and readout noise was predominant over the shot noise leading to a SNR gain lower than the theoretical value.

Figure 7 shows the result of the extension of the conventional and averaged Rayleigh imaging to the turbulent methane/air flame. Figure 7a, b displays the Rayleigh signals (corrected for laser sheet non-uniformities), while Fig. 7c, d shows the SNR distributions associated with the aforementioned Rayleigh images; the increase in SNR, for pixels that have a comparable count values, is again close to 30 %.

5 High dynamic range imaging

In imaging experiments, the finite dynamic range of a detector can be a limitation to the quality of the collected data and, in general, for a given detector and set of acquisition conditions, the SNR will increase with the intensity of the acquired signals and decrease as the signal levels decay.
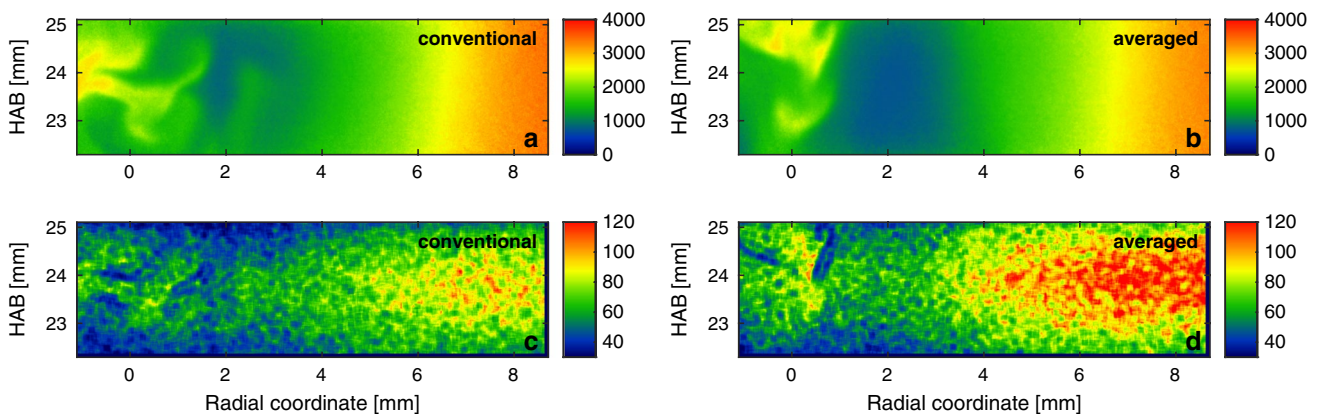

Fig. 7 **a** Rayleigh signal, in arbitrary units and corrected for laser sheet non-uniformities, of the conventional and **b** averaged Rayleigh images for the turbulent methane/air partially premixed flame (*Re*

~4000). **c** SNR distribution of the conventional and **d** averaged Rayleigh images for the turbulent methane/air partially premixed flame

This section describes an alternative method that can be implemented to increase the SNR in laser-based imaging experiments in which signals are large enough that image saturation becomes a limitation to the useful dynamic range: It exploits the high dynamic range concept presented in (Giassi et al. 2015) for steady combustion systems and extends it to unsteady ones. The method relies on the combination of multiple partially saturated images into an unsaturated one (Madden 1993; Reinhard et al. 2010), and it has been shown that the reconstructed HDR image is able to return improved SNR across the whole dynamic range, with a factor-of-two increase in low-signal regions. Experiments involving multiple synchronized lasers and detectors have been demonstrated and may be good candidates for this approach (Barlow et al. 2009; Frank et al. 2005; Fuest et al. 2012a, b, 2015; Kaiser and Frank 2009; Karpetis and Barlow 2002). The flexibility of recently developed pulse-burst laser systems (Fuest et al. 2012a, b; Papageorge et al. 2014; Patton et al. 2012a, b) may also provide enough laser energy that limited detector dynamic range becomes the main experimental limitation. To test the applicability of the concept, planar Rayleigh imaging is taken again as a test case and used to acquire a two-frame sequence of a time-varying non-reacting flow injected in air, so that an HDR image can be computed.

When dealing with HDR imaging, it is important that two main assumptions are satisfied: First, the detector must display excellent linearity and reciprocity under both unsaturated and partially saturated conditions. Second, since multiple images have to be mathematically combined into a single one, the imaged phenomena must be the same, with little or no spatial variation between frames. If this condition is not satisfied, the resulting spatial mismatch will introduce unphysical features in the HDR image. In unsteady flows, the latter condition can be avoided by ensuring that the time separation between the first and last collected image of the HDR sequence is smaller than the characteristic time scale of the phenomenon under study. The linearity of the detector used in this study has already been shown in Sect. 3. For the specific application of HDR imaging to techniques relying on pulsed lasers for illumination, the camera reciprocity loses importance since each image's recorded intensity is not determined by the camera exposure but by the energy of the laser pulse.

The experimental configuration used to test the applicability of HDR imaging to unsteady flows is a variation of the one introduced in Sect. 2. It is shown in Fig. 8 where two illuminating sheets are generated by two different lasers and sent, from opposite directions, into the probe volume where Rayleigh-scattered light is collected and imaged onto an interline-transfer CCD. Unlike the previous set of experiments, no image intensifier was used and the two images necessary for the HDR reconstruction were
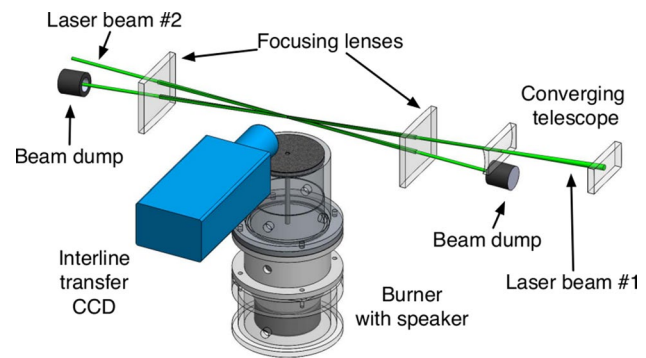

Fig. 8 Schematic diagram of the experimental setup used for the HDR planar Rayleigh scattering imaging

created by collecting the scattered light from the two separate laser shots.

The first image of the two-frame sequence was created by focusing the second harmonic of a Spectra Physics Pro-250 Nd:YAG laser into a sheet (3.3-mm height, ~35-μm FWHM beam waist thickness, 200 mJ/pulse) and sending it through a turbulent jet of dichlorodifluoromethane (Freon-12) injected into an air co-flow (4-mm nozzle diameter, 75-mm co-flow diameter). The relative Rayleigh cross sections of Freon-12 and air are 20.33 and 0.97, respectively. The average velocities of Freon-12 and air were 22 and 27 cm/s, respectively, and the flow unsteadiness was induced by a sinusoidal forcing generated with a speaker placed in the fuel plenum and driven at 30 Hz with a Stanford Research DS345 function generator (the forced flow was chosen over a turbulent one to allow for a comparison between HDR and conventionally averaged results). The second image of the sequence was created in a similar fashion with the use of a Continuum Powerlite Nd:YAG laser whose beam was focused into a sheet (6-mm height, ~140-μm FWHM beam waist thickness, 100 mJ/pulse) and sent through the same probe volume defined by the first laser sheet. The measurements were taken at a fixed height above the burner centered three diameters downstream; to avoid the laser beams entering each other's cavities, the first beam was slightly tilted and crossed the probe volume with a 2.5° angle. The camera chip was binned 2×2 pixels, and the pulse energies were chosen so that the first image saturated the detector in some areas, while the second image used a significant portion of the camera dynamic range without any saturation.[1] The interpulse separation was set to 2.5 μs; when compared to the average gas velocity, the

---

[1] The applicability of the proposed methodology to reactive flows (like the partially premixed methane/air flames described in Sect. 2) would require fluences higher than the ones that were achievable with the laser setup used in this work (ideally ~1500 J/cm^2, if the detector is used with no binning).

spatial displacement of the flow structures between the two collected frames was expected to be ~0.5 μm. This value, given the magnification of the collection optics, was well below the spatial resolution of the imaging system (the length projected onto a binned pixel was equal to 13.5 μm). While the velocity modulation induced by the speaker was not quantified, the large margin between spatial resolution and spatial shifting ensured that the two acquired frames sampled the same event.

The Rayleigh image post-processing was similar to what already described in Sect. 2, and the algorithm used for the evaluation of the ith pixel intensity of the reconstructed HDR image, H_i, is presented in Eq. (2) (Giassi et al. 2015).

$$H_i = \frac{h_i^L + \left(h_i^H/R\right)}{N_i} \qquad (2)$$

Here, h_i^L is the value of the ith pixel in the unsaturated image (low pulse energy), h_i^H is the value of the partially saturated one (high pulse energy), and N_i is the number of frames in which the pixel is not saturated (either 1 or 2 in this two-image case). The factor R accounts for the difference in laser energy between the two frames, and it was determined by taking the ratio of average signals evaluated in an interrogation region in both the unsaturated and partially saturated images where the scattered signal was uniform. To be included in the HDR reconstruction, h_i^H has to be lower than a certain threshold identifying the detector saturation, which was chosen to be 80 % of the detector full dynamic range to account for pixel blooming effects. Finally, to account for small shot-to-shot variations and non-uniformities between the two frames, the HDR result was normalized by an image resulting from a two-dimensional smoothing of the ratio between HDR and low dynamic range (LDR) results.

Figure 9a shows the resulting HDR image of the corrected Rayleigh signal with the contour plot highlighting the separation between unsaturated (right) and saturated regions (left) as determined from the raw uncorrected Rayleigh image. The signal-to-noise ratio of the images has been evaluated according to the procedure described in Sect. 3, and Fig. 9b–d shows the SNR distribution for the HDR image, the unsaturated LDR one, as well as that for a conventional two-shot average, where neither of the two images were saturated.

As expected, the SNR distribution of the LDR and conventionally averaged images depends on the signal intensity, with higher SNR localized in the high-pixel-count regions. On the other hand, the HDR image returns an overall higher SNR in regions where both exposures contribute to the final image. Furthermore, when both exposures contribute to the HDR image, the SNR in the HDR image is seen to be as good as or better than that obtained with
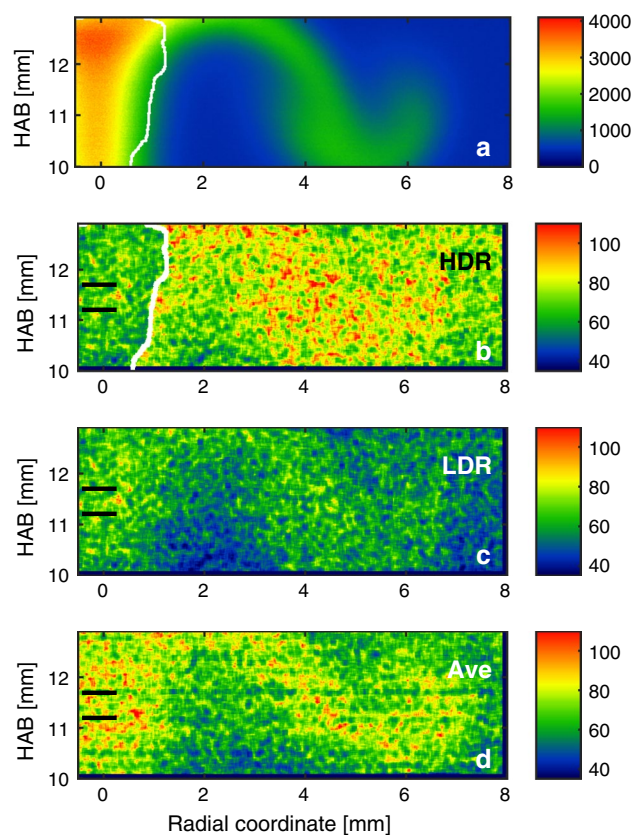

Fig. 9 **a** HDR image of Rayleigh intensity, in arbitrary units, from a Freon-12 jet injected into air (corrected for laser sheet non-uniformities); the *white line* identifies the separation between the saturated (*left*) and unsaturated areas (*right*) of the raw Freon-12 Rayleigh image. **b** SNR distributions for the HDR, **c** LDR, and **d** conventionally averaged image. The s*olid black lines* define a region over which the axial averaging has been performed to plot the *curves* shown in Fig. 10b
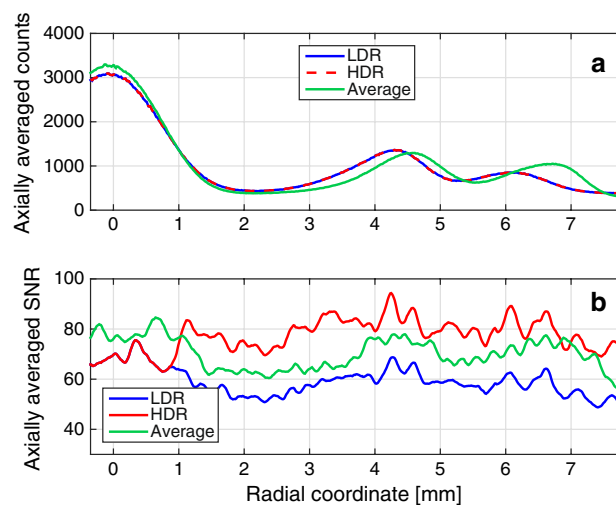

Fig. 10 **a** Comparison between the axially averaged Rayleigh counts and **b** the axially averaged SNR
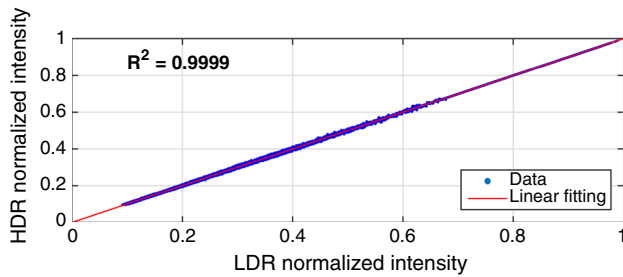
Fig. 11 HDR normalized pixel intensity as function of the LDR one

conventional averaging. Predictably, no improvement is possible in the saturated areas where information from just a single image is used. Figure 10 clarifies this conclusion by showing a radial plot of the axially averaged Rayleigh counts (Fig. 10a) and axially averaged SNR distribution (Fig. 10b) over a region defined by the black lines shown in Fig. 9. The increase in SNR of the unsaturated region is seen to be ~35 and ~15 %, when compared to the LDR and conventionally averaged image, respectively.

Finally, the verification that the HDR image carries the same quantitative information of the unsaturated one was done by plotting and comparing, pixel by pixel, the HDR image pixels intensity (normalized to the detector full dynamic range) as function of the LDR one, as shown in Fig. 11. The result shows excellent agreement, with a linear relation that has an R^2 value of 0.9999, giving confidence in the accuracy of the HDR reconstruction.

6 Conclusions

Two novel approaches to increase the SNR in laser-based turbulent imaging experiments have been demonstrated in reactive and non-reactive flows with the acquisition of planar Rayleigh scattering images. First, the averaged Rayleigh method was tested on steady and turbulent partially premixed methane/air flames, and it was shown that, by suitably timing the double exposure of an interline-transfer CCD camera with respect to the light emitted by the phosphor screen of an image intensifier, the intensifier output light could be equally distributed over the two frames of the detector so that an averaged image could be calculated. A linearity analysis was performed on both detector and intensifier, and no differences in response between the two frames could be observed when the camera was used in double-frame mode. For a given signal, the SNR falloff of the intensifier occurred above 7.5 V and for this reason, the measurements in this work were obtained with gains between 6.5 and 7 V. To avoid uncertainties associated with the randomness of turbulent features, the approach was initially tested on a steady partially premixed methane/air

flame: The comparison between conventional and averaged Rayleigh results showed that the SNR of the latter was 30 % higher than the former. The extension of the technique to a turbulent flame confirmed the same SNR increase.

The second method discussed the high dynamic range technique, and it showed how HDR imaging could be extended and applied to time varying/unsteady systems. Planar Rayleigh scattering has been used to acquire a two-frame sequence of an unsteady jet of Freon-12 injected in air so that an HDR image could be reconstructed. The results showed that the quantitative information carried by the HDR image was the same as the LDR one while providing a SNR ~15 % higher than the one obtained with conventional averaging.

The selection of one method over the other depends mainly on the specific experimental setup. The averaged Rayleigh approach can be quickly applied to imaging systems already equipped with intensifiers and interline-transfer CCDs, after the verification of the linearity of both components. Despite its higher complexity (in terms of required equipment), the HDR approach can similarly be adapted to those systems already predisposed to accommodate its hardware requirements. Depending on the number of images used for the HDR reconstruction, as well as the level of partial saturation, SNR improvements higher than the one shown in this work are likely to be expected.

References

Barlow RS, Wang GH, Anselmo P, Sweeney MS, Hochgreb S (2009) Application of Raman/Rayleigh/LIF diagnostics in turbulent stratified flames. Proc Combust Inst 32:945–953. doi:10.1016/J.Proci.06.070

Eckbreth AC (1996) Laser diagnostics for combustion temperature and species, 2nd edn. Gordon and Breach Publishers, Amsterdam

Frank JH, Kaiser SA, Long MB (2005) Multiscalar imaging in partially premixed jet flames with argon dilution. Combust Flame 143:507–523

Fuest F, Barlow RS, Chen JY, Dreizler A (2012a) Raman/Rayleigh scattering and CO-LIF measurements in laminar and turbulent jet flames of dimethyl ether. Combust Flame 159:2533–2562. doi:10.1016/J.Combustflame.2011.11.001

Fuest F, Papageorge MJ, Lempert WR, Sutton JA (2012b) Ultrahigh laser pulse energy and power generation at 10 kHz. Opt Lett 37:3231–3233

Fuest F, Barlow RS, Magnotti G, Dreizler A, Ekoto IW, Sutton JA (2015) Quantitative acetylene measurements in laminar and turbulent flames using 1D Raman/Rayleigh scattering. Combust Flame 162:2248–2255

Giassi D, Liu B, Long MB (2015) Use of high dynamic range imaging for quantitative combustion diagnostics. Appl Opt 54:4580–4588

Hoess P, Karlheinz F (2000) Time-integrated phosphor behavior in gated image intensifier tubes. In: International symposium on

optical science and technology. International society for optics and photonics, pp 23–28

Hoess P, Karlheinz F (2001) Response of very-fast-decay phosphors in image intensifier tubes for CCD readout devices. In: 24th international congress on high-speed photography and photonics. International society for optics and photonics, pp 127–132

Irum I, Shahid MA, Sharif M, Raza M (2015) A review of image denoising methods. J Eng Sci Technol Rev 5:41–48

Jain A, Kerhalkar MS, Ahmed MM, Shaikh TA, Prabhu MR, Sasikala UT, Majumder SK, Guha P, Uche UM, Christian OH (2014) Review on denoising technique for the AWGN signal introduced in a stationary image. Int J Eng Sci Invent 3:01–10

Janesick JR (2001) Scientific charged-coupled devices. SPIE Press, Bellingham

Kaiser SA, Frank JH (2009) Spatial scales of extinction and dissipation in the near field of non-premixed turbulent jet flames. Proc Combust Inst 32:1639–1646

Kalt PAM, Long MB (2014) OMA—image processing for Mac OS X. http://www.oma-x.org. Accessed May 2016

Kaminski CF, Long MB (2002) Multidimensional diagnostics in space and time. In: Kohse-Hoinghaus K, Jeffries JB (eds) Applied combustion diagnostics. Taylor and Francis, London, pp 224–251

Karpetis AN, Barlow RS (2002) Measurements of scalar dissipation in a turbulent piloted methane/air jet flame. Proc Combust Inst 29:1929–1936. doi:10.1016/S1540-7489(02)80234-6

Madden BC (1993) Extended intensity range imaging. Technical report, GRASP Laboratory, University of Pennsylvania

Miles R, Lempert W (1990) Two-dimensional measurement of density, velocity, and temperature in turbulent high-speed air flows by UV rayleigh scattering. Appl Phys B 51:1–7. doi:10.1007/BF00332317

Papageorge MJ, McManus TA, Fuest F, Sutton JA (2014) Recent advances in high-speed planar Rayleigh scattering in turbulent jets and flames: increased record lengths, acquisition rates, and image quality. Appl Phys B 115(2):197–213

Patton RA, Gabet KN, Jiang N, Lempert WR, Sutton JA (2012a) Multi-kHz mixture fraction imaging in turbulent jets using planar Rayleigh scattering. Appl Phys B Lasers Opt 106:457–471. doi:10.1007/S00340-011-4658-1

Patton RA, Gabet KN, Jiang N, Lempert WR, Sutton JA (2012b) Multi-kHz temperature imaging in turbulent non-premixed flames using planar Rayleigh scattering. Appl Phys B Lasers Opt 108:377–392. doi:10.1007/S00340-012-4880-5

Product datasheet, Proxitronic Funk GmbH & Co.KG (1998) Bensheim, Germany

Reinhard E, Ward G, Pattanaik S, Debevec P (2010) High dynamic range imaging: acquisition, display and image-based lighting. Morgan Kaufmann Publishers, San Francisco, CA, USA

Shao L, Yan R, Li X, Liu Y (2014) From heuristic optimization to dictionary learning: a review and comprehensive comparison of image denoising algorithm. IEEE Trans Cybern 44:1001–1013. doi:10.1109/TCYB.2013.2278548

Zhao FQ, Hiroyasu H (1993) The applications of laser Rayleigh-scattering to combustion diagnostics. Prog Energy Combust Sci 19:447–485. doi:10.1016/0360-1285(93)90001-U

Zhou J, Qiu Y, Wu X (2013) Relation between signal-to-noise ratio of UV image intensifiers and voltage of MCP. In: Image processing and photonics for agricultural engineering, Proc SPIE, vol 8761, pp 87610T-1–87610T-5